

**TURBULENT FLOW OF LIQUID STEEL AND ARGON BUBBLES
IN SLIDE-GATE TUNDISH NOZZLES
PART I: MODEL DEVELOPMENT AND VALIDATION**

Hua Bai and Brian G. Thomas

Hua Bai, Senior research engineer, is with the Dow Chemical Company, 2301 N. Brazosport Blvd., Freeport, TX 77541, and Brian G. Thomas, Professor, is with the Department of Mechanical and Industrial Engineering, University of Illinois at Urbana-Champaign, 1206 W. Green Street, Urbana, IL 61801

ABSTRACT

The quality of continuous-cast steel is greatly affected by the flow pattern in the mold, which depends mainly on the jets flowing from the outlet ports in casting with submerged tundish nozzles. An Eulerian multiphase model has been applied to study the three-dimensional turbulent flow of liquid steel with argon bubbles in slide-gate tundish nozzles using the finite-difference program CFX. Part I of this two-part paper describes the model formulation, grid refinement, convergence strategies, and validation of this model. Equations to quantify average jet properties at nozzle exit are presented. Most of gas exits the upper portion of the nozzle port while the main downward swirling flow contains very little gas. Particle Image Velocimetry (PIV) measurements are performed on a 0.4-scale water model to determine the detailed nature of the swirling velocity profile exiting the nozzle. Predictions with the computational model agree well with the PIV measurements. The computational model is suitable for simulating dispersed bubbly flows, which exist for a wide range of practical gas injection rates. The model is used for extensive parametric studies of the effects of casting operation conditions and nozzle design, which are reported in Part II of this two-part paper.

KEY WORDS: Multiphase, Multi-fluid, Turbulence, Numerical model, PIV, Continuous Casting, Argon injection, Slide-gate nozzle, Jet characteristics, finite-difference, water model

I. INTRODUCTION

Tundish nozzle geometry is one of the few variables that is both very influential on the continuous casting process and relatively inexpensive to change. Slide-gates are commonly used to control the flow rate, but their off-center throttling generates asymmetry. Argon injection into the nozzle is widely employed to reduce nozzle clogging. These variables all affect flow in the nozzle, and subsequently in the mold. Poor flow in the mold can cause many quality problems ^[1-3]. There is thus great incentive to understand quantitatively how these variables affect the flow pattern in the nozzle and the jet characteristics exiting the outlet ports, as a step towards optimizing steel quality.

Previous modeling studies of flow in nozzles have focused on single-phase flow. Hershey, Najjar and Thomas ^[4, 5] assessed the accuracy of two- and three- dimensional finite-element simulations of single-phase flow in a bifurcated submerged entry nozzle (SEN) through comparison with velocity measurements and water modeling observations. They demonstrated the reasonable accuracy of separating the nozzle and mold calculations and using 2-D simulations for some symmetrical flows. Their work was later extended ^[6] to perform an extensive parametric study of single-phase symmetrical flow in the nozzle. Wang ^[3] employed a 3-D finite-element single-phase model of a complete tundish nozzle, (including the upper tundish nozzle, the slide-gate, and the SEN), to confirm the asymmetrical flow caused by the slide gate. Yao ^[7] used a finite-volume method to model flow through the SEN and the mold together.

Experimental works have reported the importance of two-phase flow in nozzles when argon injected. Tsai ^[8] observed the partial vacuum pressure at the upper portion of SEN in the water experiments, and found that proper argon injection might avoid the vacuum pressure and hence reduce the air aspiration. Heaslip et al. ^[9] performed water model experiments to investigate the use of injected gas to carry alloying elements into the liquid. Burty et al. ^[2] observed a flow pattern transition from dispersed bubbly flow to “annular” flow where gas and liquid separates. A criterion for this transition was developed based on water model experiments through stopper-rod nozzles that depends on both gas flow rate and liquid flow. Sjöström et al. ^[10] performed an experimental study of argon injection and the aspiration of air into a stopper rod using liquid steel,

and found that air aspiration could be reduced by increasing the argon flow rate or pressurizing the stopper. Little work has been reported on the mathematical modeling of the two-phase flow in nozzles, although some studies have been published on two-phase flow in the ladle ^[11, 12] and mold ^[13, 14].

Several different methods have been developed to simulate multiphase flow in the continuous casting process. Thomas et al. ^[15] tracked the trajectories of individual bubbles through the liquid steel in a mold using a Lagrangian approach for particle transport. The effect of the argon bubbles on the steel flow pattern was neglected, so, the results only apply to low argon flow rates. Bessho et al. ^[13] and Thomas and Huang ^[14] modeled the gas-liquid flow in the mold by solving the 3-D, incompressible, steady-state, mass and momentum conservation equations for the liquid phase. The buoyancy of the gas bubbles was taken into account by adding an extra force term in the liquid momentum equation in the vertical direction. Bubble dispersion in the gas-liquid mixture due to turbulent transport and diffusion was modeled by solving a transport equation for the continuum gas volume fraction. To simplify the problem, no momentum equation was solved for the gas phase. Instead, the bubbles were assumed to reach their steady-state terminal velocity immediately upon entering the domain.

An enhancement of this procedure is the Eulerian “homogeneous model” ^[16] which still solves only a single set of transport equations, but adopts mixture properties where the density and viscosity are proportional to the volume fraction of the phases. The volume fractions vary with and sum to one in each cell. A model of this type was applied to model the transient flow phenomena in continuous casting of steel ^[17].

Another form of multiphase flow model, originally developed by Hirt ^[18], was developed specifically to track the movement of gas-liquid interfaces through the domain. The gas-liquid interface is defined by the volume fraction of liquid, which is equal to one or zero everywhere in the domain except the interface. Its movement is calculated by solving an additional transport equation. Again, transport equations are solved only for the liquid phase. This method is usually

used for free surface flows and stratified flows, such as non-dispersed flow or tracking individual bubble formation^[19], and possibly for modeling annual flow in nozzles.

Creech^[20] investigated the turbulent flow of liquid steel and argon bubble in the mold using the multi-fluid Eulerian multiphase model, in which one velocity field for the liquid steel and a separate velocity field for the gas phase are solved. The momentum equation for each phase is affected by the other phase through inter-phase drag terms. This approach is adopted in current work.

In this first part of a two-part paper, a three-dimensional finite difference model is developed to study the time-averaged two-phase turbulent flow of molten steel and argon bubbles in slide-gate tundish nozzles using the multi-fluid Eulerian multiphase model. Based on a grid resolution study, an optimum grid is chosen to allow both accurate prediction and economical computing resource. Fast convergence is achieved by using proper initial guess and numerical strategies. Jet characteristics at the port outlets are quantified with weighted-average properties such as jet angle, jet speed, back flow zone and biased mass flow. The computational model is then verified by comparing its simulation with measurements using PIV (Particle Image Velocity) technology on a 0.4 scale water model. A parametric study using the model is presented in Part II of this two-part paper.

II. PROCESS DESCRIPTION

A schematic of part of the continuous casting process is depicted in Figure 1, showing the tundish, tundish nozzle and mold regions. In a typical slab casting operation, the liquid steel flows from the tundish, through the ceramic tundish nozzle, and exits through bifurcated ports into the liquid pool in the mold. The domain of interest of this work consists of the upper tundish nozzle (UTN), the slide-gate plates and the submerged entry nozzle (SEN). Between the two segments of the tundish nozzle, the flow rate is regulated by moving a “slide gate”, which restricts the opening. Argon bubbles are injected through holes or pores in the nozzle wall to mix into the flowing liquid steel. The nozzle outlet ports are submerged below the surface of the molten steel in the mold to

avoid interference with the interface between the steel and the slag layers which float on top. Flow from the nozzle is directed by the shape of the ports and the angles of the port walls. The nozzle controls the flow pattern developed in the mold by governing the speed, direction, swirl and other characteristics of the liquid jet entering the mold.

III. MODEL FORMULATION

The computational domain for simulating flow through a typical slide-gate nozzle is shown in Figure 2 with its boundary conditions. The top of the nozzle is attached to the tundish bottom and the outlet ports exit into the continuous casting mold. Flow in this nozzle is inherently three-dimensional, two-phase and highly turbulent. The Reynolds number, based on the nozzle bore diameter (D), is typically of the order of 10^5 . A multi-fluid Eulerian multiphase model is used to simulate the time-average flow of argon bubbles in liquid steel. Each phase has its own set of continuity and momentum equations. Coupling is achieved through an empirical inter-phase drag between liquid steel and argon bubbles.

A. Governing equations

The governing equations of mass and momentum balance for the liquid phase are

$$\frac{\partial(v_{li}f_l)}{\partial x_i} = 0 \quad (1)$$

$$\rho_l \frac{\partial(v_{lj}v_{li}f_l)}{\partial x_j} = -f_l \frac{\partial p_l}{\partial x_i} + \frac{\partial}{\partial x_j} \left[f_l (\mu_l + \mu_t) \left(\frac{\partial v_{li}}{\partial x_j} + \frac{\partial v_{lj}}{\partial x_i} \right) \right] + c_{lg} (v_{gi} - v_{li}) \quad (2)$$

and for the gas phase

$$\frac{\partial(v_{gi}f_g)}{\partial x_i} = 0 \quad (3)$$

$$\rho_g \frac{\partial(v_{gj}v_{gi}f_g)}{\partial x_j} = -f_g \frac{\partial p_g}{\partial x_i} + \frac{\partial}{\partial x_j} \left[f_g \mu_g \left(\frac{\partial v_{gi}}{\partial x_j} + \frac{\partial v_{gj}}{\partial x_i} \right) \right] + f_g (\rho_l - \rho_g) g_i + c_{lg} (v_{li} - v_{gi}) \quad (4)$$

where the indices i and $j = 1, 2, 3$ represent the x , y and z directions, $v_i = \{u, v, w\}$ are the velocity components in these three directions, the subscripts l and g donate the liquid and gas phases, f is volume fraction, ρ is density, μ is molecular viscosity and μ_t is the turbulent (or eddy) viscosity. Repeated indices imply summation. Because the density of the gas is 3-4 orders of magnitude smaller than that of the liquid, turbulence in the gas phase is neglected. The standard, two-equation K - ε turbulence model is chosen for liquid phase turbulence, which requires the solution of two additional transport equations to find the fields of turbulent kinetic energy, K , and turbulent dissipation, ε ^[21],

$$\rho_l \frac{\partial(f_l v_{lj} K)}{\partial x_j} = \frac{\partial}{\partial x_j} \left(f_l \left(\mu_l + \frac{\mu_t}{\sigma_K} \right) \frac{\partial K}{\partial x_j} \right) + \mu_t f_l \frac{\partial v_j}{\partial x_i} \left(\frac{\partial v_i}{\partial x_j} + \frac{\partial v_j}{\partial x_i} \right) - \rho_l f_l \varepsilon \quad (5)$$

$$\rho_l \frac{\partial(f_l v_{lj} \varepsilon)}{\partial x_j} = \frac{\partial}{\partial x_j} \left(f_l \left(\mu_l + \frac{\mu_t}{\sigma_\varepsilon} \right) \frac{\partial \varepsilon}{\partial x_j} \right) + C_1 \frac{\varepsilon}{K} \mu_t f_l \frac{\partial v_j}{\partial x_i} \left(\frac{\partial v_i}{\partial x_j} + \frac{\partial v_j}{\partial x_i} \right) - C_2 \rho_l f_l \frac{\varepsilon^2}{K} \quad (6)$$

The turbulent viscosity μ_t is calculated from the turbulent kinetic energy and dissipation by

$$\mu_t = C_\mu \rho_l \frac{K^2}{\varepsilon} \quad (7)$$

The above equations contain five empirical constants that appear to produce reasonable behavior for a wide range of flows ^[22] when given standard values as follows:

$$C_1 = 1.44, \quad C_2 = 1.92, \quad C_\mu = 0.09, \quad \sigma_K = 1.00, \quad \sigma_\varepsilon = 1.30$$

There is an obvious constraint that the volume fractions sums to unity

$$f_l + f_g = 1 \quad (8)$$

Equations 1-8 represent 12 equations with 13 unknowns (u, v, w, p, f for each phase, and μ, K, ε for liquid turbulence). The final equation needed to close the system is given by the simple constraint that both phases share the same pressure field:

$$p_l = p_g = p \quad (9)$$

The last term of momentum equation (2) and (4) accounts for inter-phase transfer of momentum between the liquid steel and the argon bubbles. Here, c_{lg} denotes the inter-phase momentum exchange coefficient, which is related to the relative velocity of the two phases by

$$c_{lg} = \frac{3}{4} \frac{C_D}{D} f_g \rho_l |v_{li} - v_{gi}| \quad (10)$$

where D is the bubble diameter. The non-dimensional drag coefficient C_D is a function of the bubble Reynolds number, defined as Re_{bub}

$$Re_{bub} = \frac{\rho_l |v_l - v_g| D}{\mu_l} \quad (11)$$

The function $C_D(Re_{bub})$ is determined experimentally, and is known as the drag curve:

$$C_D = \frac{24}{Re_{bub}} (1 + 0.15 Re_{bub}^{0.687}) \quad (13)$$

This equation, known as the ‘‘Allen regime’’, is valid for $0 \leq Re_{bub} \leq 500 - 1000$. Analysis of the results reveals that most bubbles in this study are in the Stokes regime, represented by the first term in Equation 13.

B. Inlet boundary conditions

Over the inlet plane at the top of the nozzle, velocity is fixed to a constant corresponding to the chosen flow rate. A uniform normal velocity profile is assumed, which is a reasonable approximation of the 1/7 power-law profile expected in turbulent pipe flow. Turbulent kinetic energy and turbulent dissipation at the inlet are specified using the semi-empirical relations for pipe flow ^[23]. The liquid volume fraction is set to 1.0 over this top boundary.

C. Gas injection

Argon gas is injected along the lower portion of the inner surface of the upper tundish nozzle (UTN) wall. At this boundary, the normal velocity of the gas phase is specified from the gas flow rate divided by the region area. The liquid fraction is set to zero. Calculations show that gas injected through the ‘‘hot’’ ceramic wall heats up to 99% of the molten steel temperature even before it reaches the liquid steel, as seen in Appendix I. Thus, the argon gas injection flow rate

used in the numerical model is the “hot” argon flow rate. This is simply the product of the “cold” argon flow rate measured at STP (Standard Temperature of 25°C and Pressure of 1 atmosphere) and the factor of gas volume expansion due to the temperature and pressure change, β , which is about 5^[1]. Gas injection may also be characterized by the average gas volume fraction, $\overline{f_g}$ which can be found from

$$\overline{f_g} = \frac{\beta Q_g}{\beta Q_g + Q_l} \quad (14)$$

where Q_g is the gas injection flow rate at STP and Q_l is the liquid flow rate through the nozzle, found by multiplying the casting speed by the cross sectional area of the strand.

D. Wall Boundary

The boundary condition along the nozzle walls is the standard K - ε “wall law”. This approach can capture the steep velocity gradient in the boundary layer near the wall without using excessive grid refinement. Normal velocity components are set to zero and the tangential velocity profile is defined by an empirical correlation based on the shear stress^[16]

$$V_t = -\left(C_\mu^{1/2} K\right)^{1/2} y^+ \quad \text{for } y^+ < y_0^+ \quad (15)$$

$$V_t = \frac{-\left(C_\mu^{1/2} K\right)^{1/2}}{\kappa} \log(E y^+) \quad \text{for } y^+ \geq y_0^+ \quad (16)$$

where V_t is the velocity tangential to the wall, E is the log-layer constant (9.7930), κ is the Von-Karman constant (0.419), y_0^+ is the cross over point between the viscous sub-layer and the logarithmic region, and is the upper root of

$$y_0^+ = \frac{1}{\kappa} \log(E y_0^+) \quad (17)$$

and y^+ is the non-dimensional distance normal to the wall,

$$y^+ = \frac{(\rho_l C_\mu^{1/2} K)^{1/2}}{\mu_l} n \quad (18)$$

where n is the distance normal to the wall. More details on the wall law implementation can be found elsewhere ^[16].

E. Outlet boundary condition

Setting proper boundary conditions at the outlet ports of the nozzle requires caution because the flow is not fully developed. This problem can be avoided by extending the modeling domain into the mold, but this greatly increases the computational requirements. Previous modeling of single-phase 2-D flow in nozzles has demonstrated the accuracy of setting zero normal gradients for all variables on the outlet ports ^[4-6]. Results from this approach compared favorably with experimental observations and with a combined SEN/mold model ^[4,6].

This work also adopts zero normal gradients for all variables except pressure, which is fixed to the hydrostatic pressure based on the SEN submergence depth. This reference pressure is reasonably close to the actual pressure at the nozzle ports, and has little influence on the solution except for convergence. The alternate “mass flow boundary” condition in CFX is unreasonable for this problem because it requires the mass flow rate from each port to be specified and always produces vertical jet angles of 0°.

IV. SOLUTION METHODOLOGY

A numerical grid with body-fitted coordinates is used to create the complex geometry of the nozzle domain. This was accomplished using multiple blocks, which are connected together to form an efficient structured system of equations for the entire complex geometry of the domain. The standard slide-gate nozzle geometry, shown in Figure 2, has 34,000 cells in total 74 blocks. The governing equations (Eq. 1-8) are discretized using the finite difference method and solved using the commercial finite difference program CFX version 4.2 by AEA Technology ^[16].

Grid resolution is chosen to allow both accurate and economical calculations. Figure 3 illustrates sections through the three different grid resolutions investigated: coarse, standard, and refined, with 17,028, 34,000, and 126,448 total cells respectively. The CPU times for 1000

iterations are 1.33, 2.45 and 9.42 hours respectively on the SGI Origin 2000 supercomputer at NCSA at University of Illinois at Urbana-Champaign. Figure 4 compares the solutions of velocity and volume fraction at the vertical centerlines along the entire nozzle and along the port outlet plane. The coarse grid predicted different profiles than did the standard and refined grids, especially for the volume fraction. Predictions with the standard grid are reasonably close to those of the refined grid but require only a quarter of the CPU time. Thus the standard grid was chosen as optimal for the remainder of this work.

To achieve faster convergence, a single-phase solution is obtained first and used as an initial guess for the 2-phase flow simulation. For some cases with a high gas injection volume fraction, the gas injection flow rate must be gradually increased to avoid convergence problems. For most cases, 1000 to 2000 iterations are needed to achieve a fully converged solution with scaled residuals of less than 10^{-4} . The scaled residual is the ratio of the root-mean-square residual error in a given governing equation at the current iteration to that at the second iteration. A typical convergence history for all of the scaled residuals is shown in Figure 5(A). The history of each solution variable at a monitoring point ($x=0.0299\text{m}$, $y=0.0627\text{m}$, $z=0.0664\text{m}$) is shown in Figure 5(B). The predicted values become very stable after 400 iterations while all scaled residuals fall below 10^{-4} .

A common problem in turbulent flow simulation is rapid divergence, where the residuals suddenly increase to extremely large numbers and the solver crashes. This problem is often due to the cross diffusion terms in the K transport equation (Equations 5) that contain ε and the terms in the ε equation (Equations 6) that contain K . This source of divergence was avoided by “deferred correction” in CFX ^[16], which turns off these terms for the first 500 iterations and then linearly increases them to their full values by the end of the next 500 iterations.

V. TYPICAL RESULTS

Simulation results for the nozzle in Figure 2 with the standard grid in Figure 3 and the Standard conditions in Table 1 are plotted in Figures 6 and 7 which show velocity vectors, argon gas distribution and pressure distribution respectively. Recirculation zones are found in three regions: 1) immediately under the slide plate, 2) in the cavity of the slide-gate, and 3) in the upper portion of the nozzle ports, as shown in Figure 6. In each of these regions, the velocities are relatively low at the recirculation center, and a relatively high volume fraction of gas is collected. The highest liquid velocity region is found through the slide-gate due to the throttling effect.

The flow condition leaving the nozzle ports directly affects flow in the mold and therefore the steel quality. The jets flow out of the ports with a strong vortex or swirl, as shown in Figures 6 (C) and (D). Each jet splits into two parts as it leaves the port: 1) a strong downward jet of molten steel jet which contains very little gas and 2) a weaker jet from the upper portion of the port. The latter contains a high percentage of gas and is directed upward due to the buoyancy of the bubbles. The vortex pattern and the swirl rotational directions depend on many factors such as the slide-gate opening size, slide-gate orientation, nozzle geometry, gas injection, as well as clogging, and will be further discussed in Part II of this paper.

Figure 7 shows a contour plot of the pressure distribution. While regulating the liquid steel flow, the slide-gate creates a local flow restriction which generates a large pressure drop. The lowest pressure is found in the SEN just beneath the slide gate, so joint sealing is very important there to avoid air aspiration if a vacuum occurs. A vacuum occurs if the minimum pressure falls below zero (gage). The minimum pressure is affected by argon injection, tundish bath depth, casting speed, gate opening and clogging, and is reported elsewhere ^[24]. The pressure plot in Figure 7 is also an example of the successful avoidance of a vacuum with the help of argon injection.

VI. MULTIPLE STEADY-STATE SOLUTIONS

The highly turbulent flow in nozzles is inherently time-dependent. The flow patterns predicted with the steady-state turbulent flow model shown in Equations 1-9 are time-averaged behavior. In previous experimental studies with a bifurcated nozzle with large rectangular ports ^[4], three different jet vortex patterns were observed to be relatively stable. The flow pattern periodically “flipped” between 1) a single clockwise strong swirl, 2) a single counterclockwise strong swirl, and 3) two small symmetric swirls, as observed when looking directly into the port. The pattern with two small symmetric swirls was the most unstable and lasted the shortest time between “flipping”. This time-dependent behavior can be captured by the steady-state turbulent flow simulation in this work.

Figure 8 shows the vortex patterns predicted in a full 3-D SEN for the conditions of Hershey et al ^[4] (Table I). All three flow patterns in Figure 8 are fully converged solutions for the same simulation condition. Only the initial guess for the velocity field was varied. Starting from a symmetric initial guess of zero velocity generates two small symmetric swirls, as shown in Figure 8(C). This matches the solution obtained in earlier work with symmetry imposed ^[4]. An initial guess with small uniform horizontal velocity components to the right converges to a solution with one large counterclockwise swirl and one small clockwise swirl at the center plane. When flow exits the port, the flow pattern evolves into a single vortex rotating counterclockwise, as shown in Figure 8(A). Switching the initial velocity components to the left reverses the resulting vortex pattern, as shown in Figure 8(B). These different converged solutions to the same problem likely represent local minima in the residual error space. When such multiple solutions are encountered, convergence difficulties are likely. This situation appears to occur in nature also, which explains the transient oscillation between flow patterns observed in the water models.

In this work, the full nozzle domain is always modeled for two reasons. Firstly, the slide-gate nozzle often has little symmetry to exploit (for example, a 45° orientated slide-gate has no symmetry at all). Secondly, modeling a quarter of the SEN based on the geometric symmetry forces the solution to converge to the symmetric flow pattern, so multiple solutions cannot be

observed. The finding of multiple steady flow patterns suggests that slight changes in operating conditions (such as gate opening and clogging) are likely to cause great changes in the most stable flow pattern, especially when near critical conditions.

VII. JET CHARACTERISTICS

The tundish nozzle affects steel quality through its influence on the flow pattern in the mold. As a step towards investigating the effect of nozzle design and operation conditions on the flow pattern in the mold, the jet characteristics are quantified here in terms of average jet angle, jet speed, back-flow zone, and biased mass flow. The jet characteristics are calculated from the numerical solution at the port outlet plane. These jet properties are computed using weighted averages based on the local outward flow rate. The values associated with the low-velocity back-flow zone (where flow reenters the nozzle) are ignored. These definitions follow those of previous work for single-phase flow ^[6], with modifications to account for the gas phase. The local liquid velocity magnitude at cell i on the nozzle port is defined as:

$$U_i = \sqrt{(u_l)_i^2 + (v_l)_i^2 + (w_l)_i^2} \quad (19)$$

Weighted average liquid velocity at the nozzle port in the x-direction:

$$\overline{u_l} = \frac{\sum_{i \text{ (if outflow)}} [(u_l)_i U_i (\Delta y)_i (\Delta z)_i (f_l)_i]}{\sum_{i \text{ (if outflow)}} [U_i (\Delta y)_i (\Delta z)_i (f_l)_i]} \quad (20)$$

Weighted average liquid velocity at the nozzle port in y-direction:

$$\overline{v_l} = \frac{\sum_{i \text{ (if outflow)}} [(v_l)_i U_i (\Delta y)_i (\Delta z)_i (f_l)_i]}{\sum_{i \text{ (if outflow)}} [U_i (\Delta y)_i (\Delta z)_i (f_l)_i]} \quad (21)$$

Weighted average liquid velocity at the nozzle port in z-direction:

$$\overline{w_l} = \frac{\sum_{i \text{ (if outflow)}} [(w_l)_i U_i (\Delta y)_i (\Delta z)_i (f_l)_i]}{\sum_{i \text{ (if outflow)}} [U_i (\Delta y)_i (\Delta z)_i (f_l)_i]} \quad (22)$$

Weighted average turbulence energy at the nozzle port:

$$\bar{K} = \frac{\sum_{i \text{ (if outflow)}} [K_i U_i (\Delta y)_i (\Delta z)_i (f_l)_i]}{\sum_{i \text{ (if outflow)}} [U_i (\Delta y)_i (\Delta z)_i (f_l)_i]} \quad (23)$$

Weighted average turbulence dissipation at the nozzle port:

$$\bar{\varepsilon} = \frac{\sum_{i \text{ (if outflow)}} [\varepsilon_i U_i (\Delta y)_i (\Delta z)_i (f_l)_i]}{\sum_{i \text{ (if outflow)}} [U_i (\Delta y)_i (\Delta z)_i (f_l)_i]} \quad (24)$$

Vertical Jet Angle:

$$\theta_{zx} = \tan^{-1} \left(\frac{\bar{w}_l}{\bar{u}_l} \right) = \tan^{-1} \left(\frac{\sum_{i \text{ (if outflow)}} [(w_l)_i U_i (\Delta y)_i (\Delta z)_i (f_l)_i]}{\sum_{i \text{ (if outflow)}} [(u_l)_i U_i (\Delta y)_i (\Delta z)_i (f_l)_i]} \right) \quad (25)$$

Horizontal Jet Angle:

$$\theta_{yx} = \tan^{-1} \left(\frac{\bar{v}_l}{\bar{u}_l} \right) = \tan^{-1} \left(\frac{\sum_{i \text{ (if outflow)}} [(v_l)_i U_i (\Delta y)_i (\Delta z)_i (f_l)_i]}{\sum_{i \text{ (if outflow)}} [(u_l)_i U_i (\Delta y)_i (\Delta z)_i (f_l)_i]} \right) \quad (26)$$

Jet Speed:

$$U_{jet} = \sqrt{(\bar{u}_l)^2 + (\bar{v}_l)^2 + (\bar{w}_l)^2} \quad (27)$$

Back-flow zone fraction:

$$\eta = \frac{\sum_{all \ i} [(\Delta y)_i (\Delta z)_i] - \sum_{i \text{ (if outflow)}} [(\Delta y)_i (\Delta z)_i]}{\sum_{all \ i} [(\Delta y)_i (\Delta z)_i]} \quad (28)$$

where Δy and Δz are the lengths of the cell sides, $(u_l)_i$, $(v_l)_i$, and $(w_l)_i$ are the liquid velocity components in the x , y , and z directions, and $(f_l)_i$ is the liquid volume fraction in cell i . The summation operation Σ is performed on all cells at the port exit plane with outward flow. Positive

vertical jet angle indicates downward flow while positive horizontal jet angle indicated flow towards the inner radius.

VIII. MODEL VALIDATION

A. Water Model Experiments and PIV Measurements

To verify the computational model, flow visualization and velocity measurements were made using a 0.4-scale water model of the tundish, nozzle and mold of the caster at LTV Steel (Cleveland, OH). The model and flow pattern is pictured in Figure 9 for the conditions given in Table I as “Validation Nozzle”. The PIV (Particle Image Velocimetry) system developed by DANTEC Measurement Technology was used to measure the velocity field at the plane of interest near the nozzle port. In PIV, a pulsed laser light sheet is used to illuminate a plane through the flow field which has been seeded with tracer particles small enough to accurately follow the flow. The positions of the particles in a 24x14 pixel field are recorded with a digital CCD (Charged Coupled Device) camera at each instant the light sheet is pulsed, yielding an “exposure”. The images from two successive exposures are processed to match up individual particles and calculate the vector displacement of each. Knowing the time interval between the two exposures (1.5ms), the velocity of each particle can be calculated and the velocities are combined to produce an instantaneous velocity field. In this work, this procedure was repeated every 0.533 second to obtain the complete history of the fluctuating velocity field under nominally steady conditions. To obtain a time-averaged or “steady” velocity field, the results from 50 exposures were averaged. Errors in matching up particles sometimes produce abnormal huge velocities at a single point, which are easy to recognize. Thus, before averaging, the vector plot of each exposure is examined and each abnormal vector is replaced by the average of its four normal neighbors. If the abnormal vector is at the nozzle port, only the neighbors on the outside of the nozzle port are averaged to obtain the replacement vector, because velocities inside the nozzle cannot be accurately measured.

Because the PIV measurement generates a planar velocity vector field that does not include the v-component of the velocity (y-direction, perpendicular to the light sheet), the resulting speed

measurements should be compared with calculated magnitudes based only on the u- and w- velocity components. To evaluate the direction of the jet exiting the port, a “slice jet angle” is calculated from an arithmetic average of the angles of all vectors along the port exit in the particular slice illuminated by the laser light sheet:

$$\theta_{zx-slice} = \frac{1}{N} \sum_{i=1}^n \tan^{-1} \left(\frac{(w_l)_i}{(u_l)_i} \right) \quad (29)$$

where N is the number of measuring points (PIV vectors or computational cells) on the given slice through the domain at the nozzle port exit.

Figure 10 shows typical speed histories measured at two points along the port outlet centerline, one at the middle and the other at the bottom. The corresponding time average values are also given.

B. Flow Pattern Comparisons

The flow patterns observed in the experiments with the validation nozzle agree closely with the numerical simulation results. In both the water experiments and model predictions, three main recirculation zones are observed inside the nozzle: in the cavity of the middle sliding gate plate, just below this plate, and at the two nozzle ports. A high concentration of gas collects in each of these four recirculation zones. In both the simulation and the water experiments, the jet exits the ports with a single strong vortex. No obvious “back-flow” at the nozzle port was observed for the nozzle in this experiment. This matches the numerical computation for the validation nozzle, which predicts only outward flow at the nozzle ports ($\eta=0$, Equation 28). For the port-to-bore ratio of 1.3 of this nozzle, a back-flow zone is predicted in previous work [3, 4, 6, 15] where the upper port edge and the lower port edge have the same port angles. In fact, a back-flow zone was observed for the validation nozzle, when the upper port edge was changed to 15° down to match the lower port edge. Thus, the upper port angle affects the size of the back flow zone, although it is little influence on the jet angle.

The jet entering the mold is directed approximately 29° down, as seen in Figure 9. This is very close to the vertical jet angle of 27.8° down calculated from the numerical simulation results

using Equation 25. The vortex pattern is very stable, rotating clockwise when looking directly into the left port. It matches the simulated vortex pattern shown in Figure 11. This swirl is caused by the 90° slide-gate, which directs flow down the front of the nozzle bore.

C. Velocity Comparisons

A quantitative comparison of the PIV measurements and the simulation results is made on the jet at the nozzle port exit. Unfortunately, the flow field inside the plastic nozzle could not be reliably measured, due to the curvature of the nozzle wall and partial opacity from the machining cut. Figure 12(A) shows time-averaged vector plots of the PIV-measured flow field just outside the nozzle port in the center plane. The simulated vector plots are shown in Figure 12(B) for comparison. The corresponding liquid velocity magnitudes at the port are compared in Figure 12(C). Also marked on Figure 12(C) are the “slice jet angles” defined in Equation 29. The slice jet angles differ greatly from the overall average “vertical jet angle” defined in Equation 25. The upper part of Figure 12 shows that the slice jet angle for the slice C-C through the nozzle center-plane ($y=0$ in Figure 12) is downward. The lower part of Figure 12 shows upward flow near the port edge (at $y=12\text{mm}$). The jet in this slice is upward even though the overall jet is downward. This is consistent with the 3-D swirl of the jet.

The match of the velocity magnitude and the slice jet angle between the PIV measurement and the model prediction is satisfactory except that the velocity predictions are consistently slightly larger than the measurements. This might be due to the fact that the location of the pulsed laser light sheet was manually adjusted by naked eye during the PIV experiments, and thus might not lie exactly in the desired position. Figure 11 shows how the velocity magnitude is sensitive to the slice location due to the 3-D effect of the jet vortex.

IX. DISCUSSION

A. Dispersed bubble assumption

The Eulerian multi-fluid model employed in this work assumes that the gas bubbles (dispersed phase) are spherical and well distributed with the liquid (continuous phase). Bubble

coalescence or breakup can not be modeled with this method. This model is therefore suitable for bubbly flow where the gas bubbles and liquid are well mixed but is not suitable for “annular” flow where the gas and liquid phases separate into distinct regions. Experimental studies ^[2] show that the transition from bubbly (mixed) to annular (separated) flow occurs at a high gas volume fraction, specifically, 32-46% hot gas for the standard steel casting nozzle and conditions in Table I. Annual flow in the nozzle creates strong perturbations of the mold meniscus and should be avoided ^[2]. In practice, the gas injection rate is limited by its effect on the flow pattern, and is usually less than 30% in volume. Thus, the Eulerian multiphase multi-fluid model of this work is probably suitable for most practical casting conditions.

A wide range of argon gas injection volume fractions were simulated for the standard nozzle in Table I with a 45° gate orientation. Figure 13 shows the argon volume fraction profiles across the nozzle bore on the wide face center plane at three different vertical positions. Figure 13(A) shows the gas fraction profile at the gas injection region (UTN, $z=1000\text{mm}$). Here, pure gas is found near the wall and pure liquid is found in the central region of the nozzle. Gas diffuses toward the center with increasing gas injection rate. Figure 13(B) and 13(C) shows asymmetric gas fraction profile where there is an off-center blocking effect of the slide-gate. Figure 13(B) shows the profile under the blocking gate plate ($z=800\text{mm}$) where a swirl forms. The highest gas fraction is found in the center of the swirl rather than next to the wall. Figure 13(C) shows the profile at the middle of SEN ($z=400\text{mm}$) where the profile becomes more symmetric.

The dispersed model developed in this work can neither simulate the ideal annular flow profile, nor predict the observed sudden transition to annular flow. Recent work has shown the importance of surface tension and contact angle on bubble formation, which is very different in steel and water systems ^[25, 26]. Thus, further work is needed to define this transition, which is critical to nozzle flow and determines when the present model can be used.

B. Split-jet calculation

The jet characteristics defined in Equations 23-28 are weighted average quantities over the whole port. However, two separate jets may form from the same port, depending on nozzle

geometry, argon injection and the swirl effect by slide-gate, as seen in Figure 6. The downward jet is usually an asymmetric strong vortex, containing very little gas. The upward jet has a high percentage of gas, which is directed upward due to the buoyancy and flows from the very top of the port. This matches the observation in the water model experiments. A back flow zone is found between the separate two jets where flow reenters the nozzle. Its position changes with flow pattern and time.

It is possible to calculate characteristics for the two jets on each port separately rather than treat the whole outward flow as a single average jet. To illustrate how the jet might be split for analysis purpose, an example simulation was studied. This case has a 45° gate orientation and 28% (hot) argon gas injection volume fraction. The nozzle geometry and other conditions are the same as the standard nozzle in Table I. The velocity vector plots for both ports are shown in Figure 14, including the 3D view. The jet was split into a downward-jet and an upward-jet, along the division line in Figure 14, which was based on flow pattern observations. The back flow zones do not belong to either jet, so are ignored. Calculation of the characteristics for each jet still employs the weighted average method defined in Equations 23-28, but the summation is applied over each jet region (Upward-jet or Downward-jet), and the back flow zone is ignored. The split-jet calculation results, together with the overall single-jet average results are tabulated in Table II. The following observations can be made from the table.

- The upward gas-rich jet has a very large upward vertical jet angle (over 20°).
- The vertical jet angle of the downward jet is slightly steeper than that of the single (average) jet, but is still shallower than the port angle. This shows that buoyancy has a great influence on both the downward and upward jets.
- Both the downward and upward jets are directed away from the center plane, towards opposite sides of the wide face. The downward jet is directed toward the gate opening side.
- Although the upward jets take more than 30% of the area of each port, they carry less than 10% of total liquid, due to their high gas volume fractions.

- The upward jets carry over 70% of the gas.
- Because most of the liquid is carried by the downward jets, the properties of the downward port of the split jet are similar to those of the single jet.

Jet division is somehow arbitrary and case-dependent because of the swirling behavior of the jets. It is difficult to define a general scheme to split and calculate the jet characteristics as for the single overall jet. Moreover, the single and downward jet properties are similar. Therefore, for the parametric modeling study in Part II of this paper, the single jet, Equations 23-28, is employed to characterize the properties.

X. CONCLUSIONS

An Eulerian multiphase multi-fluid model has been developed to simulate two-phase turbulent flow of liquid steel and argon bubbles in a slide-gate nozzle, using a three-dimensional finite difference method. Model predictions agree both qualitatively and quantitatively with measurements conducted using Particle Image Velocimetry on a 0.4-scale water model. The model is expected to be suitable for the dispersed bubbly flow that covers the practical range of gas injection rates. The injected gas temperature is calculated to be 99% of the steel temperature at the instant of injection, so gas heat-up does not need to be considered in the future calculations. A weighted average scheme for the overall outflow is developed to quantify jet characteristics such as jet angle, jet speed, back flow zone fraction, turbulence and biased mass flow. It is also possible to characterize the outflow from each port as two split jets. These are an upward gas-rich jet and a generally downward liquid-rich jet, which determines the overall jet properties. The model is employed to perform extensive parametric studies to investigate the effects of casting operation conditions and nozzle design, which is reported in Part II of this paper.

ACKNOWLEDGMENTS

The authors wish to thank the National Science Foundation (Grant #DMI-98-00274) and the Continuous Casting Consortium at UIUC, including Allegheny Ludlum, (Brackenridge, PA),

Armco Inc. (Middletown, OH), Columbus Stainless (South Africa), Inland Steel Corp. (East Chicago, IN), LTV Steel (Cleveland, OH), and Stollberg, Inc., (Niagara Falls, NY) for their continued support of our research, AEA technology for use of the CFX4.2 package and the National Center for Supercomputing Applications (NCSA) at the UIUC for computing time. Finally, thanks are extended to LTV Steel for use of the PIV system and to M. Assar, P. Dauby, and LTV technicians for help with the measurements..

APPENDIX I: CALCULATION OF ARGON GAS HEAT-UP THROUGH THE HOLES IN NOZZLE WALL

Numerical simulations are performed to investigate the extent of heat-up of the argon gas at the instant of injection into the molten steel through pores in the nozzle wall. The argon gas is assumed to flow through a thin channel (with diameter of 0.4mm, corresponding to a typical size for the pierced argon injection holes) across the nozzle wall (with thickness of 54mm). The FLUENT code ^[27] is used to solve the steady-state heat conduction equation including gas heat-up due to both convection and conduction, using two different radial mesh resolutions (3 and 12 cells). Both cases have 270 cells across the channel. The wall temperature (boundary condition) is linear, based on previous findings ^[28], as shown in Figure 15.

Temperature-dependent physical properties of the argon gas are assumed for density, conductivity, specific heat and viscosity ^[29]. The mass flow rate of the injected argon gas is assumed to be 0.81×10^{-6} kg/s, which corresponds to 3ml/s of “hot” argon at the steel temperature.

The computed solutions for the argon gas temperature at the centerline across the nozzle wall are plotted on Figure 5, together with the wall temperature boundary condition. It can be seen that the mesh resolution in the radial direction has little influence on the results. Both cases give almost the same profile, and the finer resolution (12 cells) gives slight lower temperature at the center of the hole than that for 3 cells cases.

The argon gas is heated to over 98% of the wall temperature within 6 mm of travel. Its temperature then linearly increases as it follows the wall temperature as it flows toward the molten

steel. The gas reaches about to 99% of the molten steel temperature before it reaches the liquid steel. The gas is only about 25°C cooler than the steel, which has a negligible effect on its expansion volume.

REFERENCE

1. Thomas, B.G., Huang, X. and Sussman, R.C., "Simulation of Argon Gas Flow Effects in a Continuous Slab Caster," Metallurgical Transactions B, vol. 25B (4) (1994), pp. 527-547.
2. Burty, M., Larrecq, M., Pusse, C., Zbaczyniak, Y., "Experimental and Theoretical Analysis of Gas and Metal Flows in Submerged Entry Nozzles in Continuous Casting" (Paper presented at 13th PTD Conference, Nashville, TN, 1995), vol. 13, pp. 287-292.
3. Wang, Y.H., "3-D Mathematical Model Simulation on the Tundish Gate and Its Effect in the Continuous Casting Mold" (Paper presented at 10th Process Technology Conference, Toronto, Ontario, Canada, 1992, Iron and Steel Society, Inc.), vol. 75, pp. 271-278.
4. Hershey, D., Thomas, B.G. and Najjar, F.M., "Turbulent Flow through Bifurcated Nozzles," International Journal for Numerical Methods in Fluids, vol. 17 (1) (1993), pp. 23-47.
5. Thomas, B.G. and Najjar, F.M., "Finite-Element Modeling of Turbulent Fluid Flow and Heat Transfer in Continuous Casting," Applied Mathematical Modeling, vol. 15 (May) (1991), pp. 226-243.
6. Najjar, F.M., Thomas, B.G. and Hershey, D., "Numerical Study of Steady Turbulent Flow through Bifurcated Nozzles in Continuous Casting," Metallurgical Transactions B, vol. 26B (4) (1995), pp. 749-765.
7. Yao, M., "Flow Simulation of Molten Steel for Immersion Nozzle Design in Continuous Casting Process" (Paper presented at Modeling and Control of Casting and Welding Processes IV, 1988, TMS), pp. 893-898.

8. Tsai, H.T., "Water Modeling on Pressure Profile in the Tundish Shroud at Flo-Con", private communication, Inland Steel, 1986.
9. Heaslip, L.J., Sommerville, I.D., A., M., Swartz, G., W.W., "Model Study of Fluid Flow and Pressure Distribution During SEN Injection - Potential for Reactive Metal Additions during Continuous Casting," Transactions of the ISS (ISSM), (August) (1987), pp. 49-64.
10. Sjöström, U., Burty, M., Gaggioli, A., Radot, J., "An Experimental Study of Argon Injection and Aspiration of Air into Stopper Rod in Continuous Casters" (Paper presented at 81st SteelMaking Conference, Toronto, Canada, 1998, Iron and Steel Society, Inc.), vol. 81, pp. 63-71.
11. Mazumdar, D. and Guthrie, R.I.L., "The Physical and Mathematical Modeling of gas Stirred Ladle Systems," ISIJ International, vol. 35 (1) (1995), pp. 1-20.
12. Neifer, M., Rödl, S. and Sucker, D., "Investigations on the Fluid Dynamics and Thermal Process Control in Ladles," Steel Research, vol. 64 (1) (1993), pp. 54-62.
13. Bessho, N., Yoda, R., Yamasaki, T., FUji, T., Nozaki, T., "Numerical Analysis of Fluid Flow in the Continuous Casting Mold by a Bubble Dispersion Model," Transactions of the ISS (ISSM), (April) (1991), pp. 39-44.
14. Thomas, B.G. and Huang, X., "Effect of Argon Gas on Fluid Flow in a Continuous Slab Casting Mold" (Paper presented at 76th Steelmaking Conference, Dallas, TX, 1993, Iron and Steel Society), vol. 76, pp. 273-289.
15. Thomas, B.G., Dennisov, A. and Bai, H., "Behavior of Argon Bubbles during Continuous Casting of Steel" (Paper presented at 80th ISS Steelmaking Conference, Chicago, 1997), pp. 375-384.
16. AEA Technology, "CFX4.2 Users Manual," (1997).
17. Huang, X. and Thomas, B.G., "Modeling of Transient Flow Phenomena in Continuous Casting of Steel," in 35th Conference of Metallurgists, vol. 23B, C. Twigge-Molecey, eds., (Montreal, Canada: CIM, 1996), pp. 339-356.

18. Hirt, C.W. and Nichols, B.D., "Volume of Fluid (VOF) Method for the Dynamics of Free Boundary," Journal of Computational Physics, vol. 39 (1981), pp. 201-225.
19. Hong, T., Zhu, C. and Fan, L.-S., "Numerical Modeling of Formation of Single Bubble Chain and Bubble Breakage due to Collision with Particle in Liquid" (Paper presented at 1996 ASME Fluids Division Conference, 1996), vol. FED 236, pp. 581-588.
20. Creech, D., "Computational Modeling of Multiphase Turbulent Fluid Flow and Heat Transfer in the Continuous Slab Casting Mold" (MS Thesis, University of Illinois at Urbana-Champaign, 1999).
21. Launder, B.E. and Spalding, D.B., Mathematical Models of Turbulence, (London Academic Press, 1972).
22. Launder, B.E. and Spalding, D.B., "Numerical Computation of Turbulent Flows," Computer Methods in Applied Mechanics and Engineering, vol. 13 (1974), pp. 269-289.
23. Lai, K.Y.M. and Salcudean, M., "Computer Analysis of Multi-Dimensional□, Turbulent, Buoyancy-Induced, Two-Phase Flows in Gas-Agitated Liquid Reactors," Computational Fluids, vol. 15 (3) (1987), pp. 281-295.
24. Bai, H. and Thomas, B.G., "Effects of Clogging, Argon Injection and Tundish Depth on Flow Rate and Air Aspiration in Submerged Entry Nozzles" (Paper presented at 83rd Steelmaking Conference, Pittsburgh, PA, 2000, Iron and Steel Society, Warrendale, PA), vol. 83, pp. 183-197.
25. Cramb, A.W. and Jimbo, I., "Interfacial Considerations in Continuous Casting," ISS Transactions, vol. 11 (1990), pp. 67-79.
26. Wang, Z., Mukai, K. and Izu, D., "Influence of Wettability on the Behavior of Argon Bubbles and Fluid Flow inside the Nozzle and Mold," ISIJ International, vol. 39 (2) (1999), pp. 154-163.
27. FLUENT Inc., "Computational Fluid Dynamics Software - FLUENT User's Guide," (1995).

28. Rackers, K.G. and Thomas, B.G., "Clogging in Continuous Casting Nozzles" (Paper presented at 78th Steelmaking Conference, 1995), pp. 723-734.
29. Beaton, C.F. and Hewitt, G.F., Physical Properties Data for the Chemical and Mechanical Engineer, (Hemisphere Publishing Co., 1989).

FIGURE AND TABLE CAPTIONS

Table I Nozzle dimension and operation conditions

Table II Comparison of one overall average jet and two separate jets

Figure 1 Schematic of continuous casting tundish, slide-gate nozzle, and mold

Figure 2 Computational domain and boundary conditions for the slide-gate nozzle

Figure 3 Grid resolutions employed (a) coarse (b) standard and (c) refined grids

Figure 4 Model predictions for various grid resolutions: (a) and (b) along vertical z-axis of the nozzle; (c) and (d) along vertical centerline through the port outlet plane

Figure 5 Convergence history for a typical 2-phase turbulence flow simulation run (a) Scaled residual histories (b) Results histories at a typical point

Figure 6 Simulated flow field for the standard nozzle and conditions in Table I: (a) Argon gas distribution (b) Velocities in center plane parallel to WF (c) Velocities in center plane parallel to NF (d) Velocities at port outlet plane

Figure 7 Predicted pressure distribution for the standard nozzle and conditions in Table I: (a) Center plane parallel to WF (b) Center plane parallel to NF

Figure 8 Three vortex patterns predicted in an SEN from different initial conditions for uniform small horizontal velocity components (a) directed right (b) directed left (c) zero

Figure 9 0.4 scale water model showing flow pattern and vertical jet angle with the validation nozzle

Figure 10 Time history of the velocity magnitude measured using PIV near centerline of port outlet plane

Figure 11 Vortex pattern at port outlet and velocity profiles at different vertical slices through the nozzle port

Figure 12 Comparison of PIV measurements and model predictions (0, 12mm from center plane of the nozzle, parallel to wide face of the mold) (a) PIV measurements (b) CFX predictions (c) magnitude comparison of PIV measurements and CFX predictions

Figure 13 Effect of gas injection on gas volume fraction across the nozzle bore on wide face center plane (45° gate orientation, 50% linear gate opening, 1m/min casting speed)

Figure 14 Flow pattern showing upward jet, downward jet and back flow zone on port outlets of the standard nozzle (45° gate orientation, 28% gas, 50% linear gate opening, 1m/min casting speed)

Figure 15 Argon gas heat-up during injection through the ceramic nozzle wall

Table I Nozzle dimensions and operation conditions

Dimension & Condition	Standard Nozzle (Steel argon)	Hershey [4] Nozzle (Water)	Validation Nozzle (Water air)
UTN top diameter (mm)	114		28
UTN length (mm)	241.5		132
Gate thickness(mm)	63		18
Gate diameter(mm)	78		28
Shroud holder thickness (mm)	100		18
SEN length (mm)	748	501.2	344
SEN bore diameter (mm)	78	76	32
SEN submerged depth (mm)	200		71-80
Port-width X port-height (mm X mm)	78 X 78	60 X 90	31 X 32
Port thickness (mm)	29	25.5	11
Port angle (down)	15°	15°	40° upper edge 15° lower edge
Recessed bottom well depth (mm)	12	13	4.8
Slide gate orientation	90°		90°
Linear gate opening (F_L)	50%		52%
Casting speed (m/min, for 0.203m x 1.321m slab)	1.00	1.01	
Liquid flow rate (l/min)	268.4	272.2	42.4
Tundish depth (mm)			400-410
Argon injection flow rate (SLPM)	10.0		2.6
Argon injection (hot) volume fraction, $\overline{f_g}$	16%	0.0%	5.8%
Argon bubble diameter (mm)	1.0		1.0

Table II Comparison of the overall average single-jet and the split-jets

Jet mode Jet	Left Port			Right Port		
	Split-jets		Single jet	Split-jets		Single jet
	Upward	Downward		Upward	Downward	
Vertical jet angle	-21.65° upward	8.30° downward	4.55° downward	-20.59° upward	7.86° downward	2.41° downward
Jet speed (m/s)	0.56	0.81	0.76	0.67	0.87	0.81
Horizontal jet angle *	-4.70°	1.86°	1.06	-1.43	2.89	2.09
Back flow zone fraction			8.3%			20.1%
Area fraction of port occupied by jet	34.0%	57.7%	91.7%	31.3%	48.6%	79.9%
Liquid flow fraction carried by jet	8.7%	48.1%	56.8%	9.2%	34.0%	43.2%
Jet gas fraction on the port	61.5%	10.9%	25.8%	61.3%	11.7%	30.7%
Gas flow fraction carried by jet	35.8%	15.1%	50.9%	37.5%	11.6%	49.1%

* Horizontal jet angle > 0 : toward the wide face opposite the opening of the gate

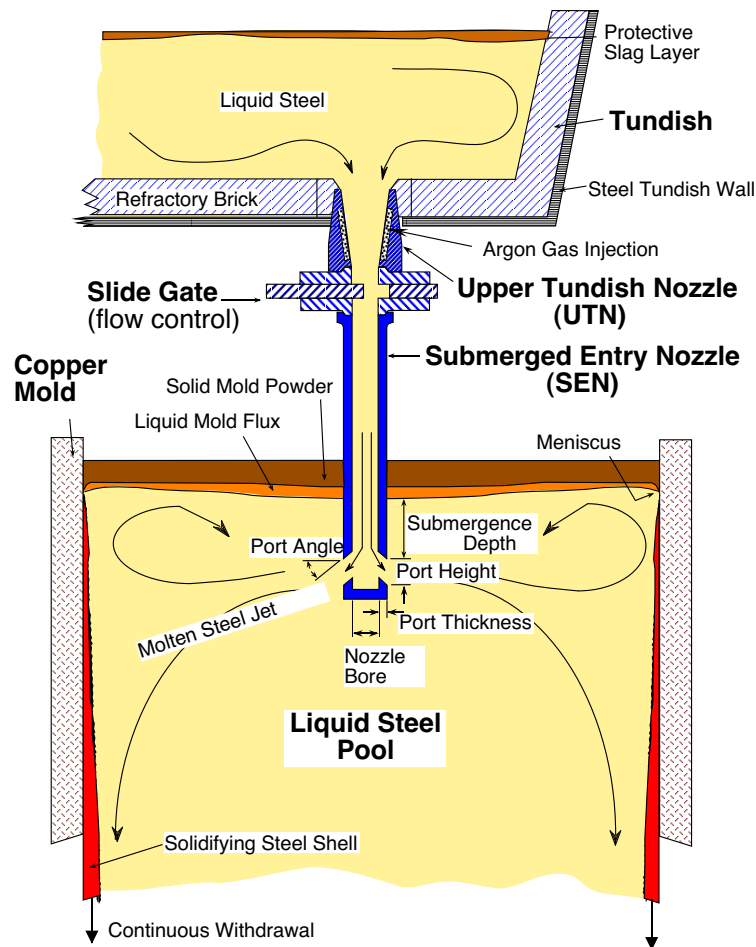


Figure 1 Schematic of continuous casting tundish, slide-gate nozzle, and mold^[4]

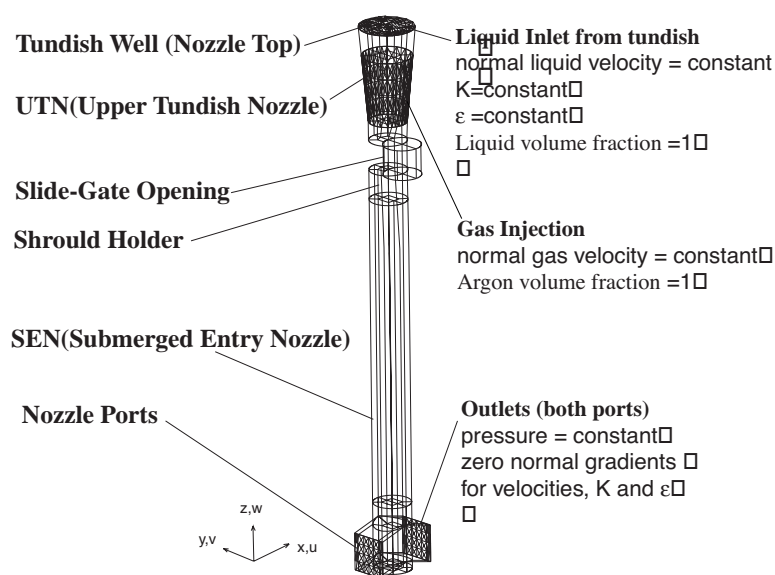


Figure 2 Computational domain and boundary conditions for the slide-gate nozzle

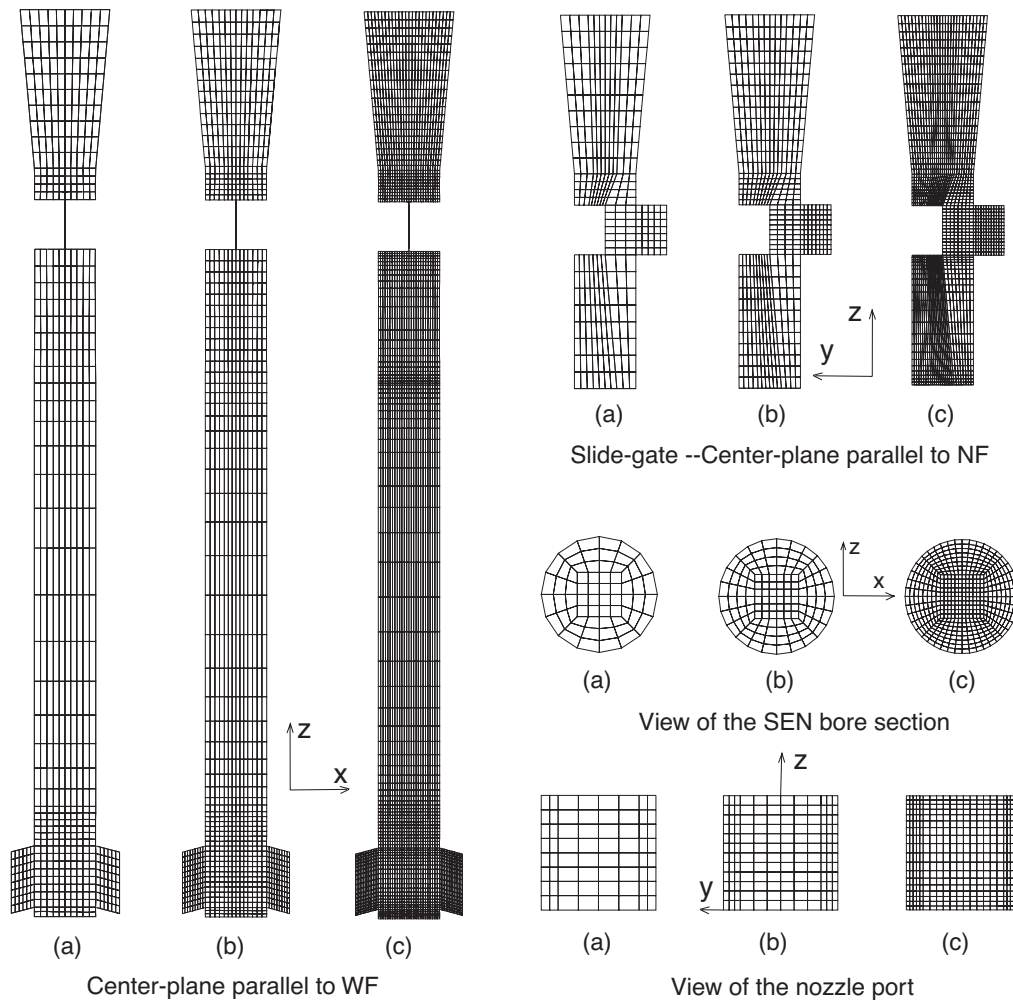


Figure 3 Grid resolutions employed (a) coarse (b) standard and (c) refined grids

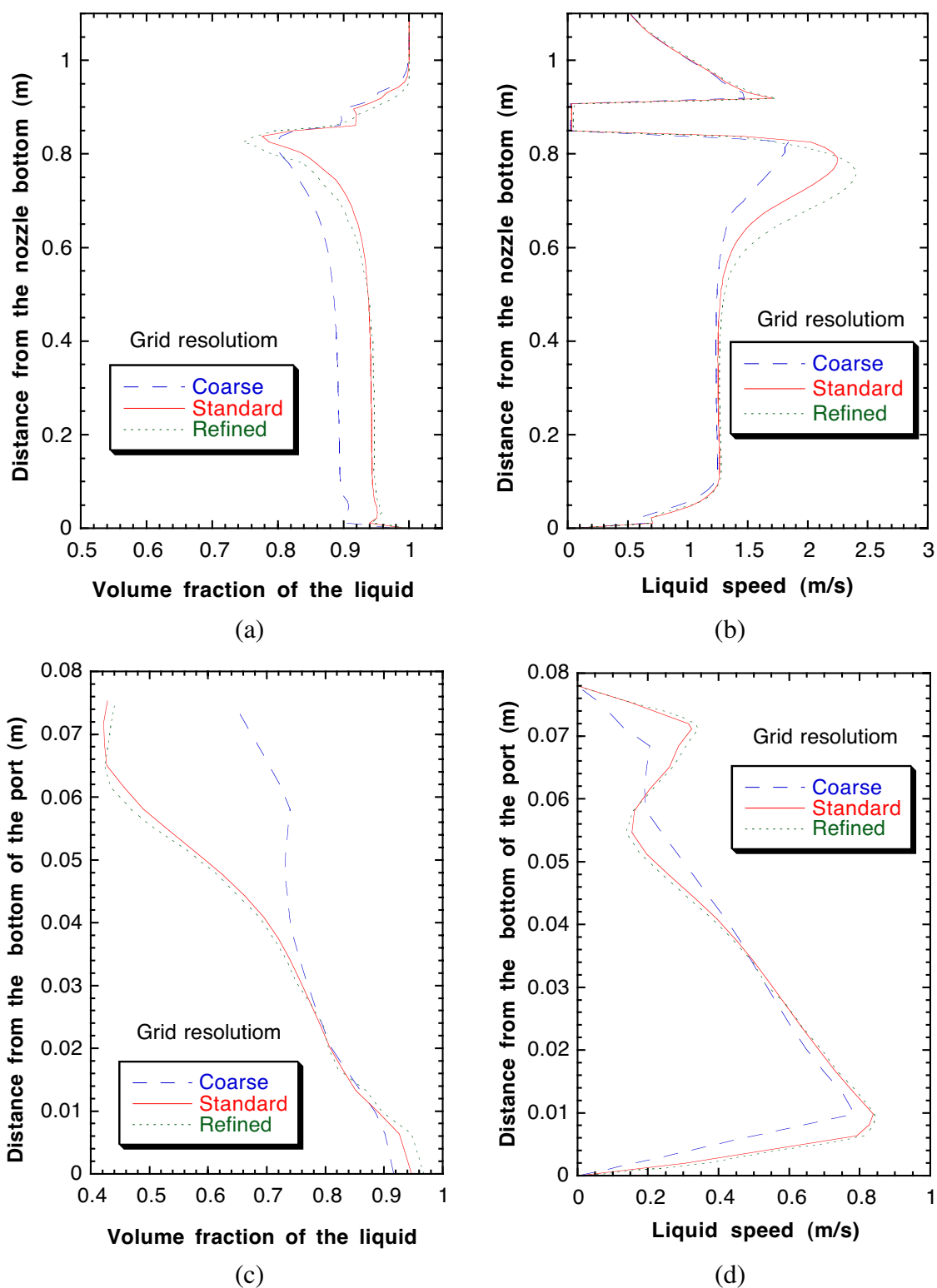


Figure 4 Model predictions for various grid resolutions: (a) and (b) along vertical z-axis of the nozzle; (c) and (d) along vertical centerline through the port outlet plane

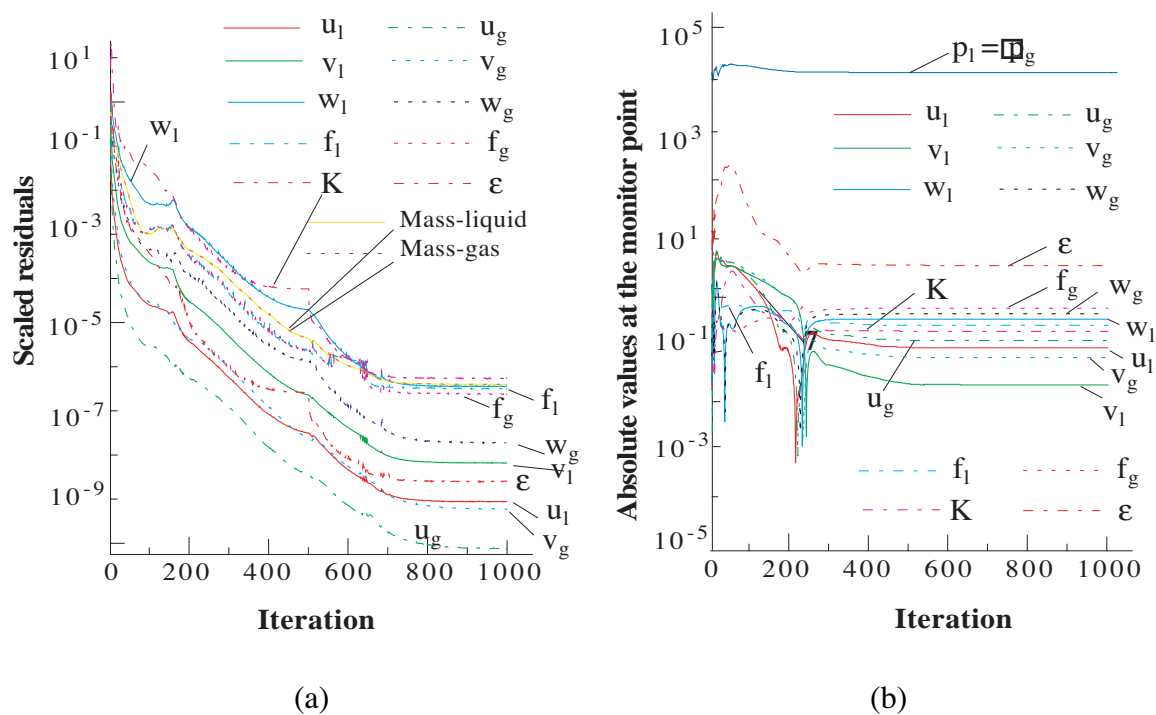


Figure 5 Convergence history for a typical 2-phase turbulence flow simulation run
 (a) Scaled residual histories (b) Results histories at a typical point

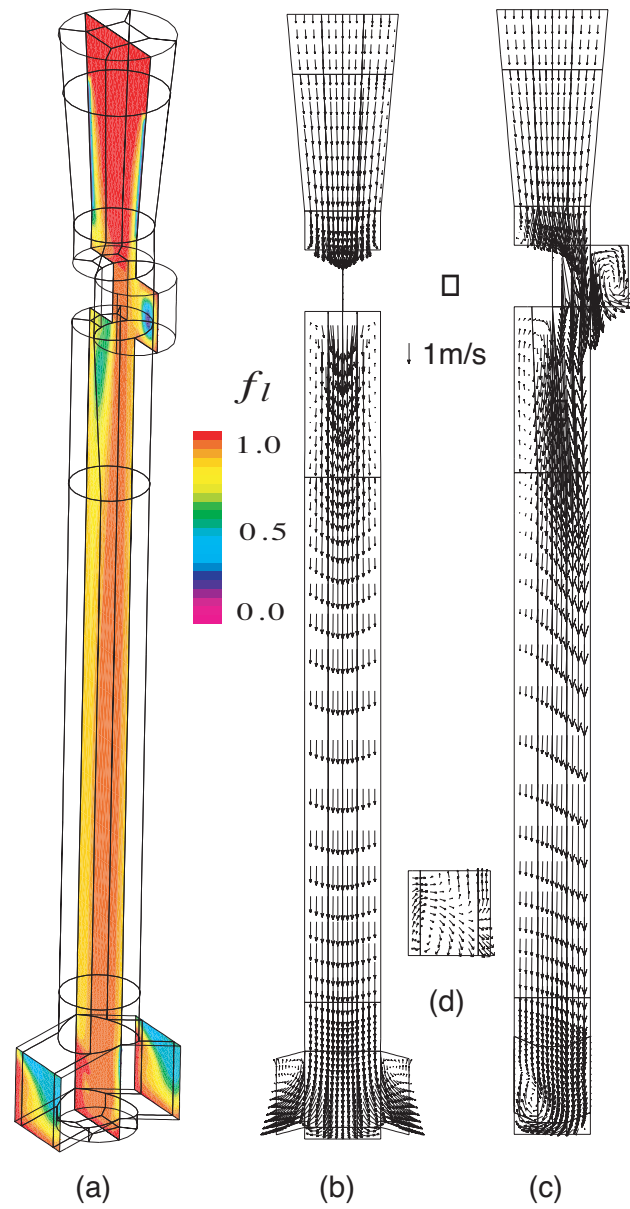


Figure 6 Simulated flow field for the standard nozzle and conditions in Table I
 (a) Argon gas distribution (b) Velocities in center plane parallel to WF
 (c) Velocities in center plane parallel to NF (d) Velocities at port outlet plane

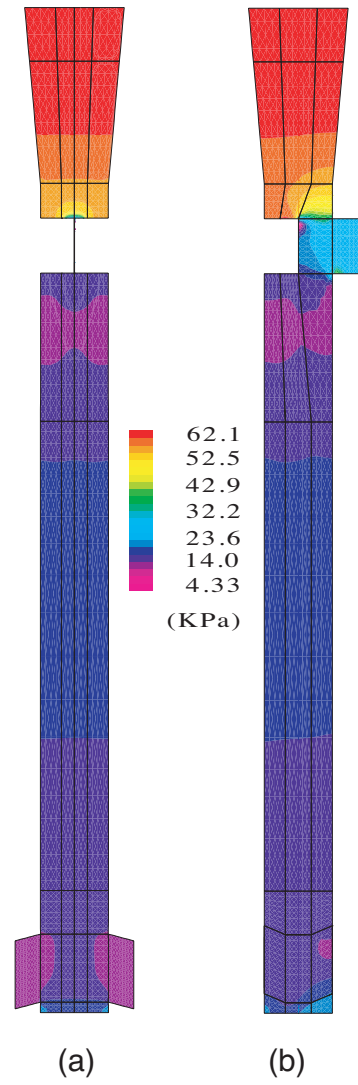


Figure 7 Predicted pressure distribution for the standard nozzle and conditions in Table I
(a) Center plane parallel to WF (b) Center plane parallel to NF

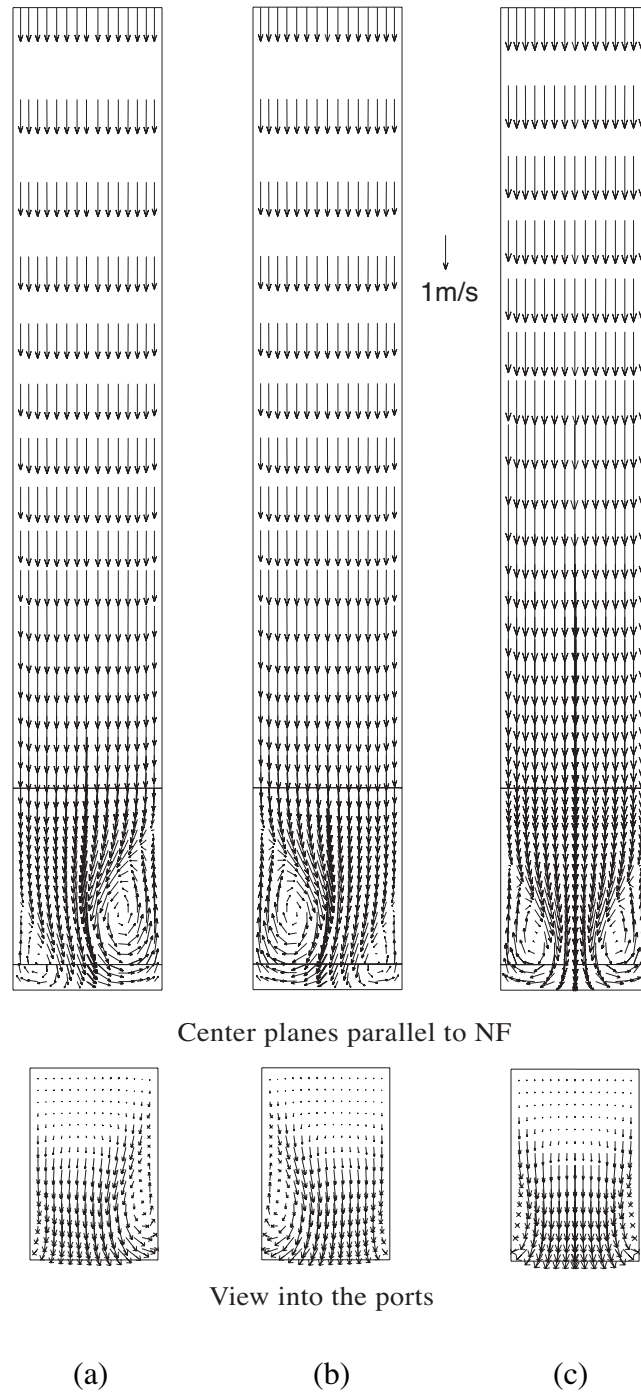


Figure 8 Three vortex patterns predicted in an SEN from different initial conditions for uniform small horizontal velocity components (a) directed right (b) directed left (c) zero

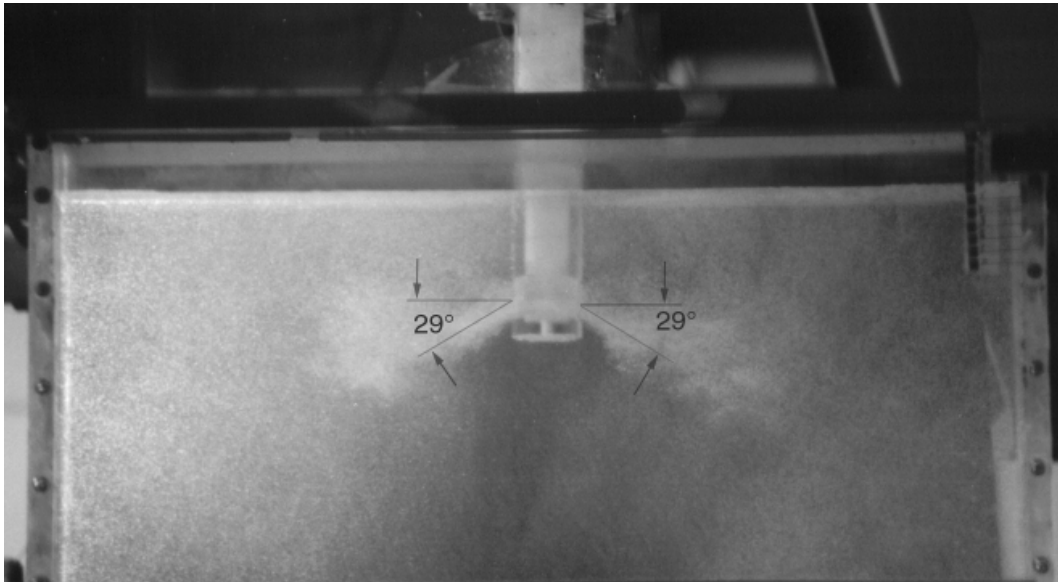


Figure 9 0.4 scale water model showing flow pattern and vertical jet angle with the validation nozzle

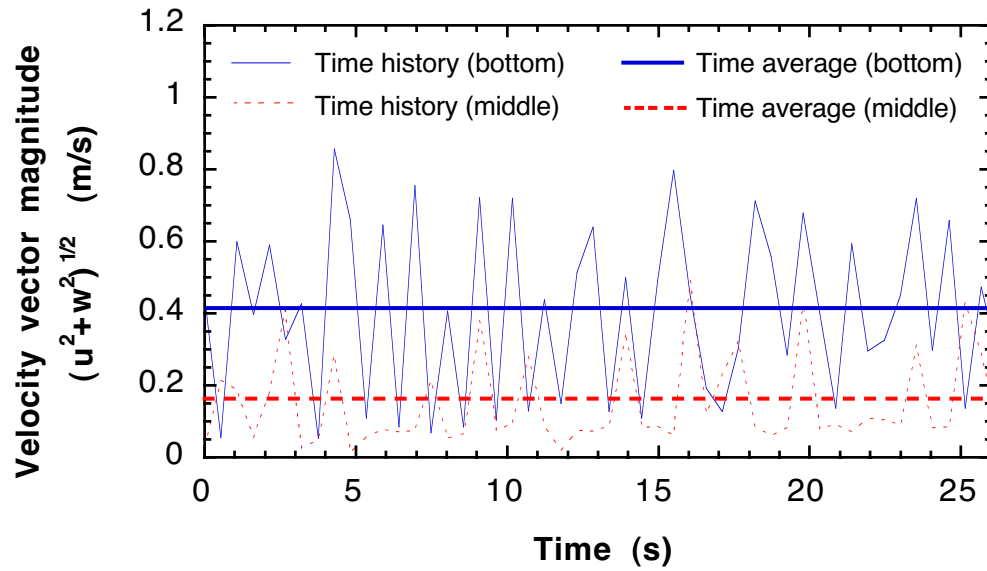


Figure 10 Time history of the velocity magnitude measured using PIV near centerline of port outlet plane

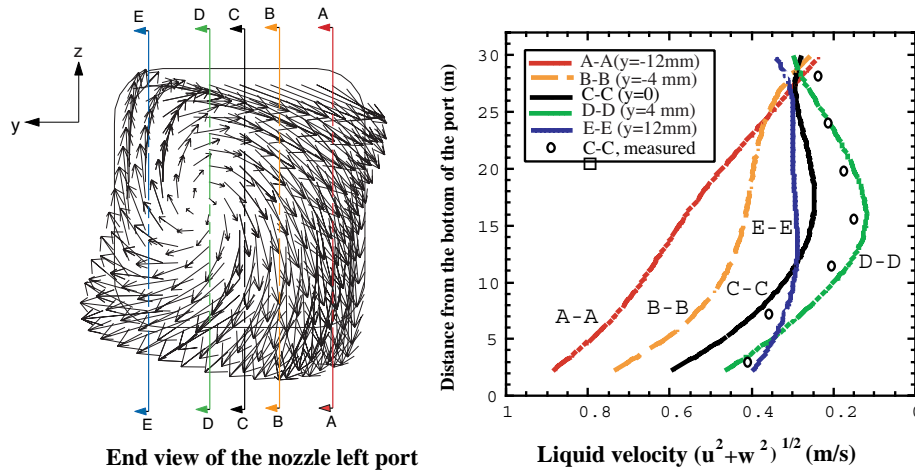


Figure 11 Vortex pattern at port outlet and velocity profiles at different vertical slices through the nozzle port

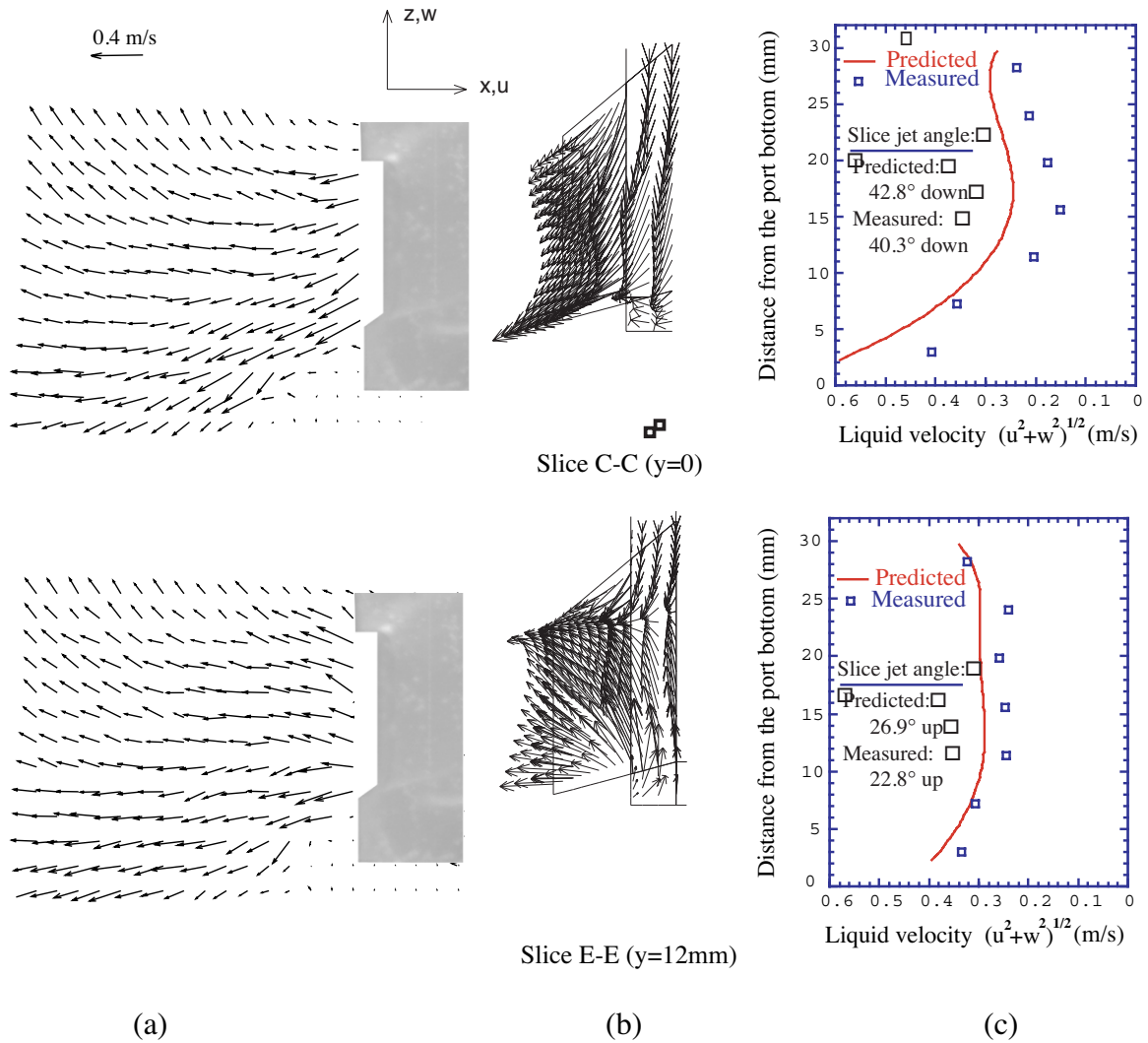


Figure 12 Comparison of PIV measurements and model predictions (0, 12mm from center plane of the nozzle, parallel to wide face of the mold) (a) PIV measurements (b) CFX predictions (c) magnitude comparison of PIV measurements and CFX predictions

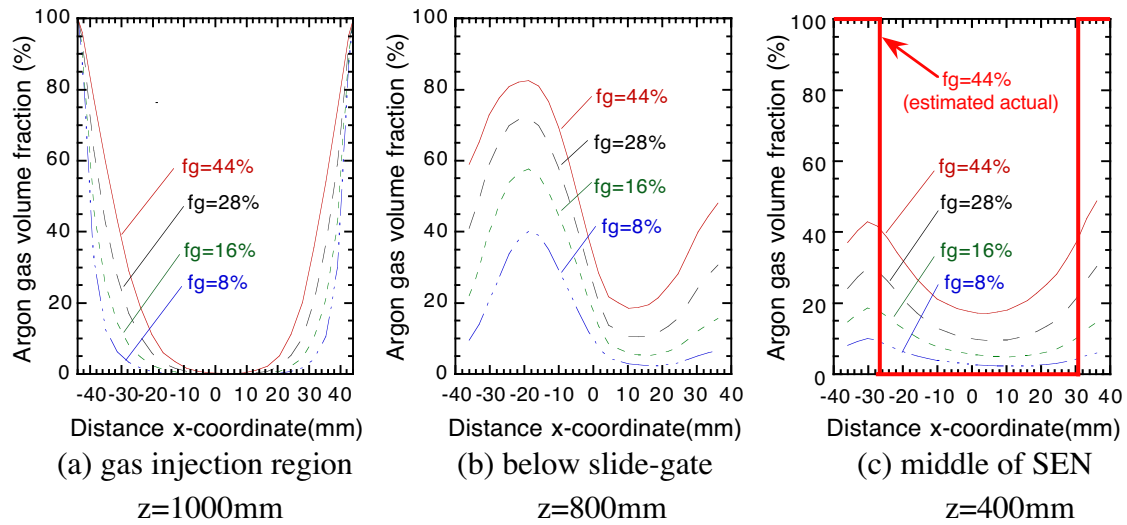


Figure 13 Effect of gas injection on gas volume fraction across the nozzle bore on wide face center plane (45° gate orientation, 50% linear gate opening, 1m/min casting speed)

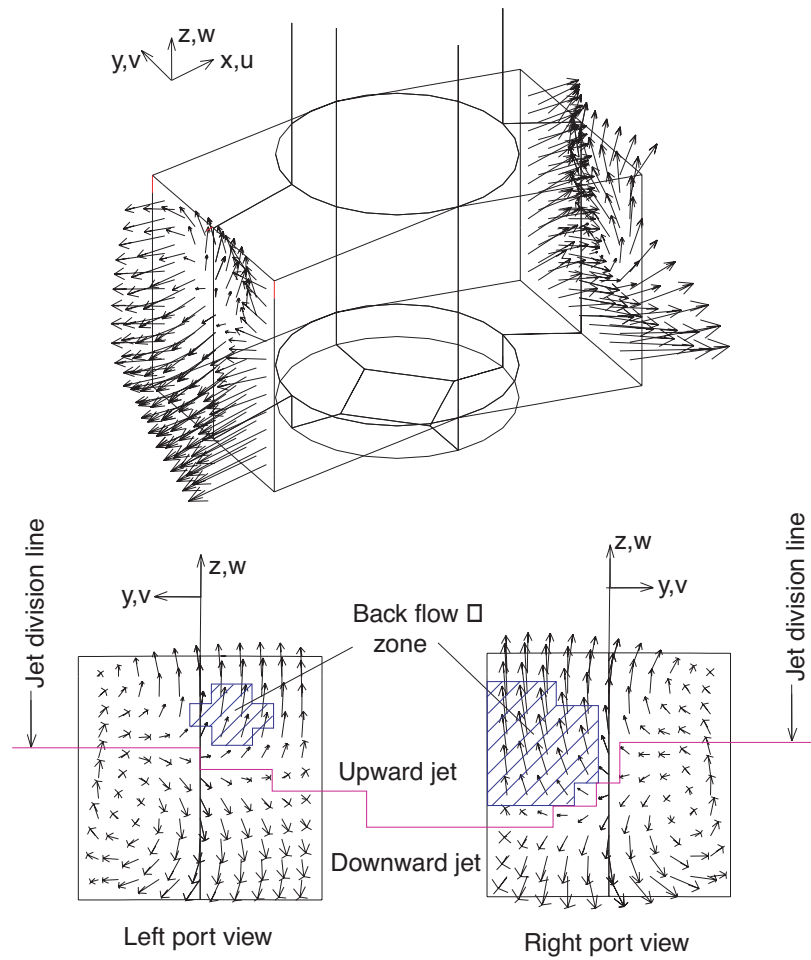


Figure 14 Flow pattern showing upward jet, downward jet and back flow zone on port outlets of the standard nozzle (45° gate orientation, 28% gas, 50% linear gate opening, 1m/min casting speed)

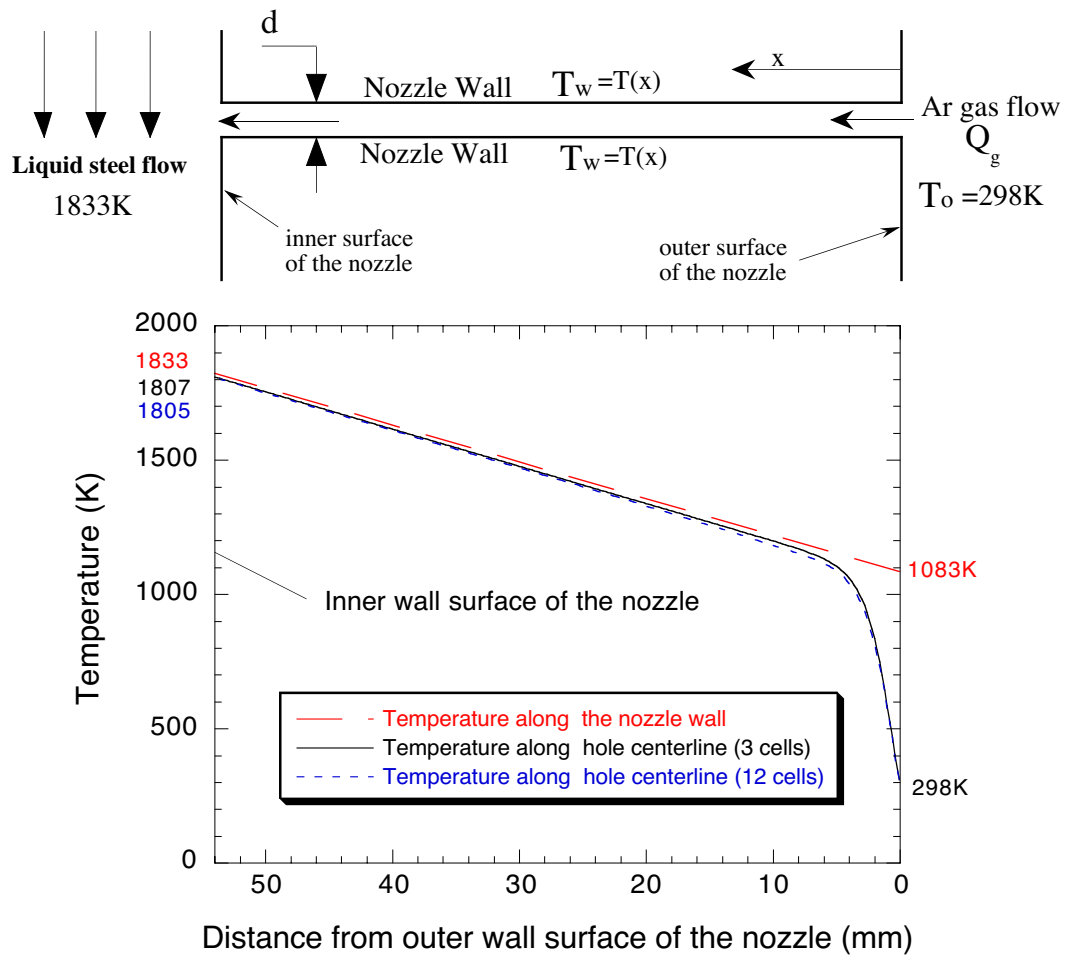


Figure 15 Argon gas heat-up during injection through the ceramic nozzle wall